Optical Engineering

OpticalEngineering.SPIEDigitalLibrary.org

Full-field fan-beam x-ray fluorescence computed tomography with a conventional x-ray tube and photon-counting detectors for fast nanoparticle bioimaging

Liang Li
Siyuan Zhang
Ruizhe Li
Zhiqiang Chen

SPIE.

Liang Li, Siyuan Zhang, Ruizhe Li, Zhiqiang Chen, "Full-field fan-beam x-ray fluorescence computed tomography with a conventional x-ray tube and photon-counting detectors for fast nanoparticle bioimaging," *Opt. Eng.* **56**(4), 043106 (2017), doi: 10.1117/1.OE.56.4.043106.

Full-field fan-beam x-ray fluorescence computed tomography with a conventional x-ray tube and photon-counting detectors for fast nanoparticle bioimaging

Liang Li,[a,b,*] Siyuan Zhang,[a,b] Ruizhe Li,[a,b] and Zhiqiang Chen[a,b]
[a]Tsinghua University, Department of Engineering Physics, Beijing, China
[b]Tsinghua University, Ministry of Education, Key Laboratory of Particle and Radiation Imaging, Beijing, China

Abstract. X-ray fluorescence computed tomography (XFCT) was performed on a high-intensity synchrotron radiation source or a pencil beam with a long exposure time due to the low emission and detection efficiency of x-ray fluorescence photons. For the first time, the feasibility and experimental results of a full-field fan-beam XFCT with a photon-counting detector array are presented. This full-field fan-beam XFCT consists of a conventional low-intensity x-ray tube, an energy-sensitive photon-counting detector array, and a tungsten pinhole collimator. A phantom containing gadolinium solution (K_α, 42.74 keV) was scanned for 30 min using a polychromatic x-ray fan beam with a third-generation computed tomography (CT) geometry. After scattering and attenuation corrections, experimental results showed that XFCT had better accuracy and performance than spectral CT. Full-field XFCT is a promising modality for biomedical imaging of exogenous molecular probes containing nanoparticles of high atomic number. [DOI: 10.1117/1.OE.56.4.043106]

Keywords: x-ray fluorescence; computed tomography; photon-counting detector; biomedical imaging; x-ray fluorescence computed tomography.

Paper 161919L received Dec. 8, 2016; accepted for publication Apr. 5, 2017; published online Apr. 20, 2017.

1 Introduction

X-ray computed tomography (CT) is important for various applications, such as medical diagnosis, industrial nondestructive testing, and security inspection. However, traditional x-ray CT image values provide information only on the linear attenuation coefficients weighted by the spectrum of the incident x-ray beam and cannot accurately identify tumors and constituents. Moreover, this drawback persists in other advanced imaging modes, including molecular imaging with dynamic contrast-enhanced CT.[1] As a state-of-the-art technique, spectral CT with multienergy-bin photon-counting detectors enables K-edge imaging. This method uses the K-absorption edge discontinuity of the attenuation coefficients of high-atomic-number elements, such as gadolinium and gold, whose K-edges lie within 50.2 and 80.7 keV, respectively. These K-edge features of contrast agents can be reconstructed and extracted for material-specific quantitative evaluation using data above and below the K-edge energy.[2] K-edge imaging aided by gold nanoparticles (NPs) has been used to detect plaque inflammation degree in coronary artery diseases.[3] However, the sensitivity of K-edge imaging depends on the scanned object size and its material composition due to beam hardening.[4]

Different from spectral CT or K-edge imaging, x-ray fluorescence computed tomography (XFCT) detects the characteristic K_α photons from a material excited by initial x-rays. XFCT is a quantitative imaging modality that reconstructs the two-dimensional or three-dimensional distribution of nonradioactive high-atomic-number NPs within a specimen, such as gold, gadolinium, and iodine.[5–7] Unlike that in K-edge CT images, the NP contrast in XFCT images is completely independent from the type of surrounding tissue.[8] Therefore, XFCT outperforms K-edge CT in imaging contrast agents at low concentrations. Bazalova et al.[8] and Feng et al.[9] proved that the contrast-to-noise ratio (CNR) of XFCT images is higher than that of transmission K-edge CT images for contrast concentrations below 0.4%. Moreover, XFCT imaging provides more depth localization than fluorescence molecular tomography,[10,11] bioluminescence tomography,[12] and x-ray luminescence CT with near-IR-emitting nanophosphor.[13,14] This advantage is important for preclinical and potential clinical applications. Therefore, with the development of x-ray-excitable NPs, XFCT is a promising modality for molecular imaging in fundamental studies, drug development, and clinical experiments.

Early XFCT is performed on high-intensity monochromatic synchrotron radiation sources with large facilities.[15–20] The pencil beam/single collimated beam from polychromatic x-ray tubes[21–27] is then used to improve the feasibility of using XFCT; however, this technique requires a long scanning time, e.g., 279 min[28] and 180 h.[29] One important reason for the low efficiency is that using a pencil beam setup requires the beam source to be shifted point by point while measuring a single slice of projection data. Similar processes of shifting on detectors are also required for a fan-beam setup with a single pixel detector.[30] Jones and Cho[31] demonstrated the simulation results of XFCT using a polychromatic

*Address all correspondence to: Liang Li, E-mail: lliang@tsinghua.edu.cn

cone-beam source with detector arrays and indicated that the total scanning time can be significantly reduced. Cong et al.[32] proposed a fan-beam XFCT setup with detector arrays and evaluated its feasibility through simulation. Apart from the shifting, these XFCT setups rely on spectrum scanning to obtain the spectral information required by Compton scatter compensation. For photon-counting detectors, spectrum scanning generates an enormous waste of x-ray dose, which aggravates the problem.

In this paper, we report the first experimental results (to the best of our knowledge) obtained using a full-field fan-beam XFCT consisting of a conventional low-intensity x-ray tube, a multibin photon-counting detector array, and a tungsten pinhole collimator.

2 Methods and Experimental Setup

As shown in Fig. 1, the XFCT process has three steps.[33] (1) The incident x-ray photons from the x-ray tube arrives at any position $\vec{r}_p$, which can be expressed as

$$I(E,\vec{r}_P) = I_0(E)\cdot e^{-\int_{l_{SP}(\vec{r})}\mu(E,\vec{r})d\vec{r}}, \tag{1}$$

where l_{SP} means the x-ray path from the x-ray source to $\vec{r}_P$ and $I_0(E)$ is the incident photon counts at energy E.

(2) X-ray fluorescence (XRF) photons are emitted isotropically from position $\vec{r}_P$ while incident x-ray photons interact with contrast agents. Its intensity can be expressed as

$$I_{\mathrm{XRF}}(\vec{r}_P) = \omega\cdot\rho(\vec{r}_P)\cdot\int_{E_K}^{E_{\max}} I(E,\vec{r}_P)\cdot\mu_{pe}^{m}(E)\mathrm{d}E, \tag{2}$$

where $\mu_{pe}^{m}(E)$ is the photoelectric mass absorption coefficient of the contrast agent, ω is the yield of fluorescence x-rays, which can be approximated as a constant, and $\rho(\vec{r}_P)$ is the concentration of contrast agent at $\vec{r}_P$ represented as a weight percent.

(3) At last, some XRF photons emitted from position $\vec{r}_p$ travel through the object and are recorded by photon-counting detectors

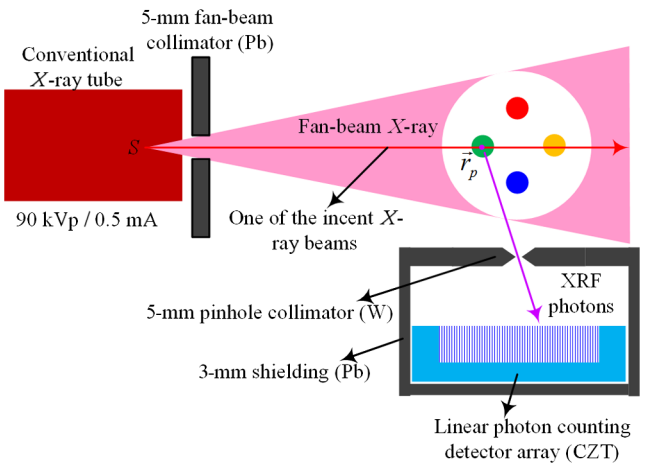

Fig. 1 Schematic of the experimental XFCT setup.

$$I_{DXF} = \int_{l_P} I_{\mathrm{XRF}}(\vec{r}_P)\cdot\int_{\mathrm{Ang}} e^{-\int_{l_{PD}(\vec{r})}\mu_{\mathrm{XRF}}(\vec{r})\mathrm{d}\vec{r}}\mathrm{d}\gamma\mathrm{d}\vec{r}_P, \tag{3}$$

where $l_{PD}(\vec{r})$ means the XRF path starting from $\vec{r}_P$ to the detector and passing the pin-hole collimator. $\mu_{\mathrm{XRF}}(\vec{r})$ is the linear attenuation coefficient of XRF photons. Ang is the solid angle range covered by the detector from $\vec{r}_P$. $l_P(\vec{r})$ denotes the line on which the emitted XRF is collected by the detector.

Then, the intensity map of generated XRF photons can be reconstructed using the iterative maximum-likelihood expectation maximization (ML-EM) algorithm as[34]

$$x_j^{(k+1)} = \frac{x_j^{(k)}}{\sum_{i=1}^{M} a_{ij}}\sum_{i=1}^{M}\frac{a_{ij}I_{DXF,i}}{\sum_{j'=1}^{N} a_{ij'}x_{j'}^{(k)}}, \tag{4}$$

where a_{ij} is the coefficient of the imaging matrix that can be calculated from the XFCT geometry, i denotes the i'th XRF photon beam, and j denotes the j'th pixel of the reconstructed map, $I_{\mathrm{XRF}}(\vec{r})$. At last, the distributions and concentration of the contrast agents, $\rho(\vec{r}_P)$, can be calculated using Eqs. (1) and (2) and $I_{\mathrm{XRF}}(\vec{r})$.

Figure 2(a) shows a photograph of our XFCT imaging setup. A low-brilliance x-ray beam (90 kV, 0.5 mA) was generated using a conventional Hamamatsu L12161-07 x-ray tube. The x-ray beam was collimated using lead plates in two directions to produce a fan beam. To reduce the total dose and scattering photons, a 0.3-mm Cu sheet was placed at the x-ray tube exit. A home-made polymethyl methacrylate (PMMA) phantom was set to rotate in precise steps using a computer-controlled motion stage, whereas the x-ray tube and the detector were stationary. The third-generation CT scanning mode was used with a rotational step of 1 deg over a full scan. At each angle view, XFCT data emitted from the

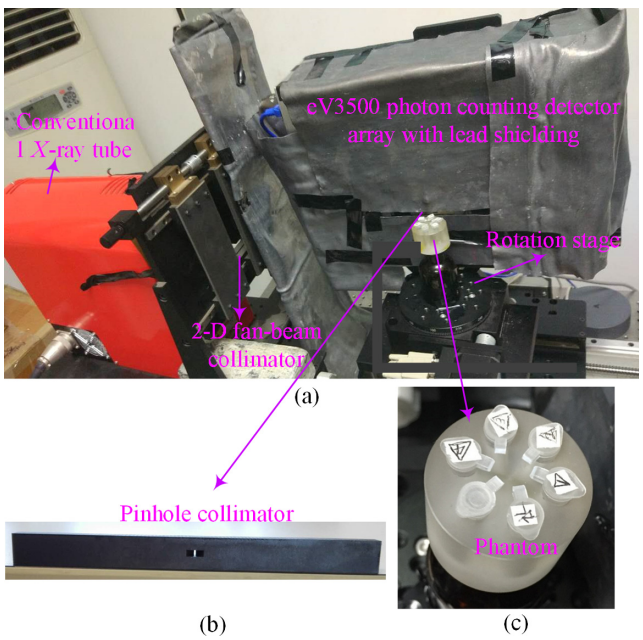

Fig. 2 XFCT imaging setup. A PMMA phantom containing gadolinium insertions was scanned on a rotating stage while being irradiated by an x-ray fan-beam.

whole phantom illuminated using the full-field fan-beam were collected by a linear photon-counting detector array (eV3500, eV PRODUCTS, Saxonburg, Pennsylvania). As shown in Fig. 2(b), a 5-mm tungsten pinhole collimator was placed before the detector. This x-ray detector used a 3-mm CdZnTe semiconductor, 256 pixels at a 0.5-mm pixel pitch, and five adjustable energy thresholds.[33] The detector was placed at a 90-deg angle to the incident x-ray beam to minimize the number of scattering photons entering the detector. Furthermore, a 3-mm lead cover was used to shield the whole detector box from x-rays coming from outside the field of view. Moreover, the same x-ray detector was repositioned behind the phantom along the beam direction to provide transmission spectral CT measurements and correct the attenuation. A PMMA phantom containing water and gadolinium solution insertions was prepared, as shown in Fig. 2(c). The insertions consisted of 1%, 2%, 3%, and 4% (weight/volume) gadolinium solutions. The phantom dimension was 35 mm in diameter.

3 Results

Figure 3 shows the sinograms (projection data, 360×256) of the XFCT experiment. Per rotation, 360 projections were acquired at a frame duration of 5 s. This scenario resulted in a total measurement time of 30 min per slice and a dose equivalent of 900 mAs. The energy thresholds were set at 35, 40, 45, 50, 70, and 90 keV. The K_α peak of gadolinium was located at 42.74 keV; hence, the data within the 40- to 45-keV energy bin were used for XFCT. Figure 3(a) shows the raw XFCT data. Although the detector was energy calibrated,[35,36] it had obvious streak artifacts because of the inconsistencies among the different detector elements. Figure 3(b) shows the gain correction results based on Fig. 3(a), wherein most of the streak artifacts were removed. However, the background was strong due to the scattered photons. The state-of-the-art XFCT systems rely on spectrum analysis to distinguish a signal from scattering; single-pixel spectrometers serve this function but generate an enormous waste of acquisition time and x-ray dose. Inspired by a method designed for single-photon emission computed tomography systems,[37] we propose to compensate for the Compton scattering based on energy bins rather than spectra. Considering that the scattering angle of each pixel is known, we can calculate the Compton scattering cross section based on the Klein–Nishina formula. With the incident tube spectrum obtained by simulation, we can determine the energy distribution of scattering photons. Based on this distribution, we can then estimate the scattering at 40 to 45 keV, which is mixed with the 42.74-keV XRF signal, by direct measurement of the scattering on nearby bins of 35 to 40 and 45 to 50 keV because XRF signals are theoretically absent. The scattering on the target energy bin can be calculated as

$$\text{Scattering}_{40\text{ to }45\text{ keV}} = \left(\frac{r_{40\text{ to }45\text{ keV}}}{r_{35\text{ to }40\text{ keV}}}\text{Scattering}_{35\text{ to }40\text{ keV}} + \frac{r_{40\text{ to }45\text{ keV}}}{r_{45\text{ to }50\text{ keV}}}\text{Scattering}_{45\text{ to }50\text{ keV}}\right) \Big/ 2, \tag{5}$$

where $r_{35\text{ to }40\text{ keV}}$, $r_{40\text{ to }45\text{ keV}}$, and $r_{45\text{ to }50\text{ keV}}$ denote the theoretical relative numbers of scattered photons, which are calculated by the energy distribution of scattering photons mentioned above. Figure 3(c) shows the scattering correction results based on Fig. 3(b), wherein the background was effectively reduced.

Figure 4 shows the XFCT reconstruction images using the ML-EM algorithm. Figure 4(a) shows the image reconstructed from the raw data of Fig. 3(b). The image shows an obvious background beside the gadolinium solution regions caused by the scattered photons. Figure 4(b) shows the image reconstructed from the scattering correction data of Fig. 3(c) where the strong background in Fig. 4(a) was effectively removed. In the 40- to 45-keV energy bin, there are averagely 18.41 photons per pixel per angle in the range of the phantom, while after the scattering correction the number drops to 3.47. Notably, XRF photons are also attenuated by the object before entering the detector. Therefore, attenuation correction should also be considered.[38] The attenuation map can be reconstructed using additional or simultaneous transmission spectral CT scan. Figure 4(c) shows the attenuation correction result based on Fig. 4(b) using the attenuation map reconstructed from the transmission spectral CT data in the 40- to 45-keV energy bin. With attenuation correction, the brightness of Fig. 4(c) is much higher than that of Fig. 4(b).

To quantify the XFCT reconstructions in Fig. 4, we calculated the average gadolinium concentration values in the regions-of-interest (ROI) marked by the red circles. The results are shown in Table 1. In the second row, the values in Fig. 4(a) are larger than the truth because the XFCT data in Fig. 4(a) contain many scattered photons that increased the calculated concentrations. After the scattering correction, the values in the third row were reduced and even smaller than the truth. As shown in the fourth row, attenuation correction can improve the reconstructed concentrations to correspond with the true values.

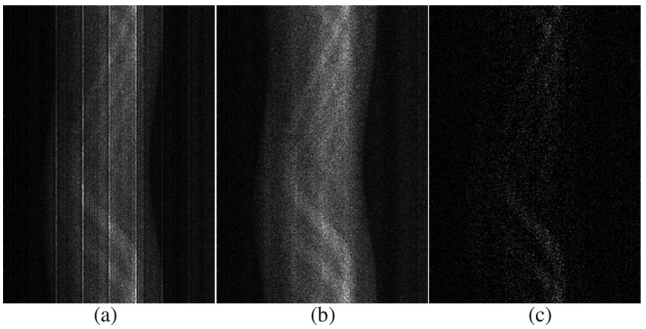

Fig. 3 Projection data (sinograms) of the XFCT: (a) raw data, (b) gain correction data based on (a), and (c) scattering correction data based on (b).

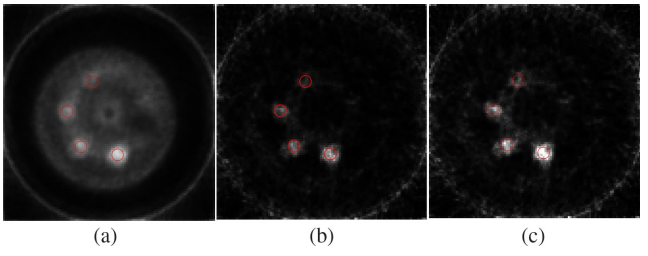

Fig. 4 (a) and (b) The ML-EM reconstruction results from the XFCT data of Figs. 3(b) and 3(c), respectively. (c) The attenuation correction result based on (b). The red circles indicate the sampling points for Table 1.

Table 1 Average gadolinium concentrations calculated from the results of Fig. 4.

Truth	1%	2%	3%	4%
Figure 4(a)	2.95%	4.49%	5.25%	7.44%
Figure 4(b)	0.61%	1.27%	1.69%	2.62%
Figure 4(c)	1.1%	2.1%	2.9%	4.6%

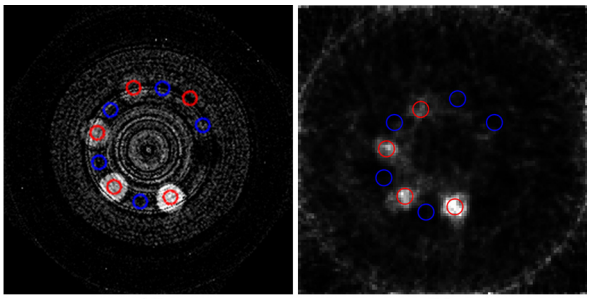

(a) (b)

Fig. 5 Comparison between spectral CT and XFCT. (a) Decomposition results of gadolinium from the spectral CT reconstruction. (b) XFCT reconstruction same with Fig. 4(c). The red circles indicate the sampling points of signal, whereas the blue ones indicate the sampling points of noise for the CNR as shown in Table 2.

Table 2 CNR comparisons between Figs. 5(a) and 5(b).

ROIs	1%	2%	3%	4%
CNR for Fig. 5(a)	0.5342	2.1075	2.7421	3.9733
CNR for Fig. 5(b)	1.1651	3.0917	4.6448	7.9373

For comparison, spectral CT imaging was performed using the same hardware and scanning parameters, e.g., kVp and mAs. The difference was that the detector array was placed against the central x-ray beam, and the energy thresholds were changed to 40, 45, 50, 55, 73, and 90 keV because the K-edge of gadolinium was located at 50.229 keV. Figure 5(a) shows the decomposition results of gadolinium from the spectral CT reconstruction. Material decomposition magnified the inconsistencies among different detector elements and resulted in strong ring artifacts.

The images in Fig. 5 were evaluated as CNR by calculating the ratio of the difference between the mean value of each ROI (red circles) and background (PMMA, blue circles) and standard deviation of the background.

As shown in Table 2, the CNR of the reconstructed XFCT image is higher than that of the corresponding spectral CT image due to its strong background. Moreover, XFCT may have a higher sensitivity than spectral CT (including K-edge CT) in molecular contrast imaging. Therefore, XFCT could be superior to spectral CT in the presence of low concentrations of contrast agents.

4 Conclusion

A study of full-field fan-beam XFCT using conventional low-intensity x-ray tube and energy-sensitive photon-counting detectors is presented. Unlike other pencil beam studies, a fan beam produced using a polychromatic x-ray tube was used to stimulate emissions of XRF photons that were collected by passing through a tungsten pinhole collimator. Thus, a whole XFCT scan can be completed within 30 min using third-generation CT geometry, which is faster than other XFCT devices that use a pencil beam with a first-generation CT geometry. Experimental results showed that scattering and attenuation correction are indispensable for highly accurate XFCT reconstruction. Moreover, the CNR of the XFCT image is higher than that of the corresponding spectral or K-edge CT image because a strong background exists adjacent to the contrast agent regions in spectral or K-edge CT images. This full-field XFCT has high sensitivity in molecular contrast imaging and is a promising modality for biomedical imaging of molecular probes. A multipinhole collimator and large detector arrays may be used in future XFCT experiments to improve the efficiency of using XRF photons.

Acknowledgments

This work was partially supported by National Natural Science Foundation of China, Award Nos: 61571256, 81427803, and 11525521; and Beijing Municipal Science and Technology Commission, Award No. Z151100003915079.

References

1. K. A. Miles, "Molecular imaging with dynamic contrast-enhanced computed tomography," *Clin. Radiol.* **65**, 549–556 (2010).
2. E. Roessl and R. Proksa, "K-edge imaging in x-ray computed tomography using multi-bin photon counting detectors," *Phys. Med. Biol.* **52**(15), 4679–4696 (2007).
3. Y. Alivov et al., "Optimization of K-edge imaging for vulnerable plaques using gold nanoparticles and energy resolved photon counting detectors: a simulation study," *Phys. Med. Biol.* **59**, 135–152 (2014).
4. E. Roessl et al., "Sensitivity of photon-counting based K-edge imaging in x-ray computed tomography," *IEEE Trans. Med. Imaging* **30**(9), 1678–1690 (2011).
5. G. F. Rust and J. Weigelt, "X-ray fluorescent computer tomography with synchrotron radiation," *IEEE Trans. Nucl. Sci.* **45**(1), 75–88 (1998).
6. G. Pratx et al., "Tomographic molecular imaging of x-ray-excitable nanoparticles," *Opt. Lett.* **35**(20), 3345–3347 (2010).
7. S. K. Cheong et al., "X-ray fluorescence computed tomography (XFCT) imaging of gold nanoparticle-loaded objects using 110 kVp x-rays," *Phys. Med. Biol.* **55**(3), 647–662 (2010).
8. M. Bazalova et al., "Investigation of x-ray fluorescence computed tomography (XFCT) and K-edge imaging," *IEEE Trans. Med. Imaging* **31**, 1620–1627 (2012).
9. P. Feng et al., "Analytic comparison between x-ray fluorescence CT and K-edge CT," *IEEE Trans. Biomed. Eng.* **61**(3), 975–985 (2014).
10. V. Ntziachristos et al., "Looking and listening to light: the evolution of whole-body photonic imaging," *Nat. Biotechnol.* **23**, 313–320 (2005).
11. X. Liu et al., "Principal component analysis of dynamic fluorescence diffuse optical tomography images," *Opt. Express* **18**(6), 6300–6314 (2010).
12. G. Wang et al., "*In vivo* mouse studies with bioluminescence tomography," *Opt. Express* **14**(17), 7801–7809 (2006).
13. X. Liu, Q. M. Liao, and H. K. Wang, "In vivo x-ray luminescence tomographic imaging with single-view data," *Opt. Lett.* **38**(22), 4530–4533 (2013).
14. C. Li et al., "X-ray luminescence optical tomography imaging: experimental studies," *Opt. Lett.* **38**(13), 2339–2341 (2013).
15. Q. Huo et al., "Sheet-beam geometry for in vivo fluorescent x-ray computed tomography: proof-of-concept experiment in molecular imaging," *Opt. Lett.* **33**(21), 2494–2496 (2008).
16. B. Deng et al., "3D elemental sensitive imaging by full-field XFCT," *Analyst* **140**(10), 3521–3525 (2015).
17. G. Fu et al., "Experimental demonstration of novel imaging geometries for x-ray fluorescence computed tomography," *Med. Phys.* **40**(6), 061903 (2013).
18. T. Takeda et al., "Fluorescent x-ray computed tomography to visualize specific material distribution," *Proc. SPIE* **3149**, 160 (1997).
19. T. Takeda et al., "Human thyroid specimen imaging by fluorescent x-ray computed tomography with synchrotron radiation," *Proc. SPIE* **3772**, 258 (1999).

20. T. Takeda et al., "X-ray fluorescent CT imaging of cerebral uptake of stable-iodine perfusion agent iodoamphetamine analog IMP in mice," *J. Synchrotron Radiat.* **16**(1), 57–62 (2009).
21. G. Pratx et al., "X-ray luminescence computed tomography via selective excitation: a feasibility study," *IEEE Trans. Med. Imaging* **29**(12), 1992–1999 (2010).
22. N. Manohar, B. L. Jones, and S. H. Cho, "Improving x-ray fluorescence signal for benchtop polychromatic cone-beam x-ray fluorescence computed tomography by incident x-ray spectrum optimization: a Monte Carlo study," *Med. Phys.* **41**(10), 101906 (2014).
23. H. M. Hertz et al., "Laboratory x-ray fluorescence tomography for high-resolution nanoparticle bio-imaging," *Opt. Lett.* **39**(9), 2790–2793 (2014).
24. P. L. Riviere et al., "Penalized-likelihood image reconstruction for x-ray fluorescence computed tomography," *Opt. Eng.* **45**(7), 077005 (2006).
25. Y. Kuang et al., "Development of XFCT imaging strategy for monitoring the spatial distribution of platinum-based chemodrugs: instrumentation and phantom validation," *Med. Phys.* **40**(3), 030701 (2013).
26. M. Bazalova et al., "L-shell x-ray fluorescence computed tomography (XFCT) imaging of Cisplatin," *Phys. Med. Biol.* **59**(1), 219–232 (2014).
27. N. Manohar, F. J. Reynoso, and S. H. Cho, "Experimental demonstration of direct L-shell x-ray fluorescence imaging of gold nanoparticles using a benchtop x-ray source," *Med. Phys.* **40**(8), 080702 (2013).
28. Y. Kuang et al., "First demonstration of multiplexed x-ray fluorescence computed tomography (XFCT) imaging," *IEEE Trans. Med. Imaging* **32**(2), 262–267 (2013).
29. A. Groll et al., "Element mapping in organic samples utilizing a benchtop x-ray fluorescence emission tomography (XFET) system," *IEEE Trans. Nucl. Sci.* **62**(5), 2310–2317 (2015).
30. B. L. Jones et al., "Experimental demonstration of benchtop x-ray fluorescence computed tomography (XFCT) of gold nanoparticle-loaded objects using lead-and tin-filtered polychromatic cone-beams," *Phys. Med. Biol.* **57**(23), N457 (2012).
31. B. L. Jones and S. H. Cho, "The feasibility of polychromatic cone-beam x-ray fluorescence computed tomography (XFCT) imaging of gold nanoparticle-loaded objects: a Monte Carlo study," *Phys. Med. Biol.* **56**(12), 3719–3730 (2011).
32. W. X. Cong et al., "X-ray fluorescence tomographic system design and image reconstruction," *J. X-Ray Sci. Technol.* **21**, 1–8 (2013).
33. L. Li et al., "Simultaneous x-ray fluorescence and K-edge CT imaging with photon-counting detectors," *Proc. SPIE* **9967**, 99670F (2016).
34. L. A. Shepp and Y. Vardi, "Maximum likelihood reconstruction for emission tomography," *IEEE Trans. Med. Imaging* **1**(2), 113–122 (1982).
35. R. Z. Li, L. Li, and Z. Q. Chen, "Spectrum reconstruction method based on the detector response model calibrated by x-ray fluorescence," *Phys. Med. Biol.* **62**, 1032–1045 (2017).
36. R. Z. Li, L. Li, and Z. Q. Chen, "Feasible energy calibration for multi-threshold photon-counting detectors based on reconstructed XRF spectra," *IEEE Trans. Radiat. Plasma Med. Sci.* **1**(2), 109–120 (2017).
37. T. Ichihara et al., "Compton scatter compensation using the triple-energy window method for single-and dual-isotope SPECT," *J. Nucl. Med.* **34**(12), 2216–2221 (1993).
38. J. P. Hogan, R. A. Gonsalves, and A. S. Krieger, "Fluorescent computer tomography: a model for correction of x-ray absorption," *IEEE Trans. Nucl. Sci.* **38**(6), 1721–1727 (1991).

Liang Li received his PhD from Tsinghua University in Beijing, China, in 2007. Currently, he is an associate professor in the Department of Engineering Physics, Tsinghua University. His research interests center on the mathematical and physical problems of x-ray imaging and its medical, industrial, and other applications.

Biographies for the other authors are not available.